

Supporting Information

CoP nanoparticles anchored on N,P dual-doped graphene-like carbon as a catalyst for water splitting in non- acid media

*Yanyan Liu,^a Yihua Zhu,^{*a} Jianhua Shen,^a Jianfei Huang,^b Xiaoling Yang^a and Chunzhong Li^{*a}*

^aKey Laboratory for Ultrafine Materials of Ministry of Education, School of Materials Science and Engineering, East China University of Science and Technology, Shanghai 200237, P. R. China.

^bDepartment of Chemistry and Biochemistry, University of California, Santa Barbara, Santa Barbara 93106, California, USA

E-mail: yhzhu@ecust.edu.cn (Prof. Y. H. Zhu), czli@ecust.edu.cn (C. Li)

*Author(s) to whom correspondence should be addressed.

EXPERIMENTAL SECTION

Materials

Nafion (5 wt%) and RuO₂ were obtained from Sigma Aldrich. Pt/C (20 wt%) was obtained from Johnson–Matthey. All other chemicals were purchased from Sinopharm Chemical Reagent Co. Ltd. All chemicals were of analytical grade and used as received without further purification. Ultrapure water (18 MΩ cm) was used for all experiments.

Synthesis of CoP@NPMG

In a typical procedure, phytic acid and melamine (molar ratio: 1: 10) were homogeneously mixed in deionized water under vigorous stirring, followed by adding CoCl₂·6H₂O and evaporating the water at 110 °C. The resultant solid samples were further dried at 80 °C under vacuum conditions overnight, followed by calcining at 900 °C for 3 h under nitrogen condition. On return to room temperature, the final product was washed with 1 M H₂SO₄ for 4 h to remove the unstable species and adjust the pH value, then washed by ultrapure water until the pH ≈ 7 and dried at 80 °C under vacuum conditions overnight. The black carbonaceous materials were named as CoP@NPMG-X. Typically, X represents the molar ratio of CoCl₂·6H₂O: phytic acid.

Synthesis of NPMG

The typical preparation is akin to that of CoP@NPMG but in the absence of any metallic sources.

Synthesis of CoP nanopartilces (CoP NPs)

CoP NPs were prepared according to literature methods.^{S11} In a typical procedure, 200 mg of Co(NO₃)₂·6H₂O and 50 mg of sodium citrate were dispersed into 100 mL deionized water and magnetic stirred for 15 min; then, 3 mL of 1 M NaOH was added dropwisely to form Co(OH)₂ precipitate. The precipitate was collected and washed with water, dried at 60 °C for 3 h. To

prepare CoP NPs, Co(OH)_2 and NaH_2PO_2 were put at two separate positions in a porcelain boat with NaH_2PO_2 at the upstream side of the furnace. The molar ration for Co:P = 1: 5. The samples were heated to 300 °C for 1 h argon atmosphere. After cooling to room temperature, the black solid was obtained.

Synthesis of CoP@rGO

In a typical synthesis, 20 mg of the graphite oxide prepared by a modified Hummers method was dispersed into a solvent mixture containing 24 ml of absolute ethanol and 0.5 ml of ultrapure water with ultrasonication for about 1 h to form a homogeneous graphene oxide (GO) dispersion. Subsequently, $\text{Co(Ac)}_2 \cdot 6\text{H}_2\text{O}$ was added into the above solution gradually under vigorous stirring. After stirring for about 3 h, 0.5 mL of $\text{NH}_3 \cdot \text{H}_2\text{O}$ (28 wt%) was introduced, and then the suspension was kept at 80 °C and stirred for 14 h. Next, the mixture was transferred to a stainless-steel autoclave and heated at 150 °C for 3 h. After the autoclave was cooled to room temperature naturally, the product was collected by centrifugation, washed with absolute ethanol and deionized water several times, and then dried in a vacuum oven at 60 °C for 24 h. Then, 20 mg of Co_3O_4 @rGO and 100 mg of sodium hypophosphite were mixed together and ground into a fine powder using a mortar. The mixture was then heated to 300 °C and maintained at 300 °C for 2 h. After cooling to room temperature naturally, the product was collected, washed with water and dried in a vacuum oven at 60 °C for 24 h. The final product was denoted as CoP@rGO.

Physicochemical Characterization

Scanning electron microscopy (SEM) was carried out on a Jeol S-4800 microscope at 5 kV equipped with an energy dispersive X-ray analyzer (EDX). Transmission electron microscopy (TEM) was carried out on a Jeol JEM-2100 microscope operating at 200 kV. Scanning

transmission electron microscopy (STEM) was carried out on a Tecnai G2 F20 S-Twin microscope operating at 200 kV. All samples subjected to TEM measurements were ultrasonically dispersed in ethanol and dropcast onto copper grids covered with a carbon film. Wide-angle X-ray diffraction (XRD) was used for powder analysis. Thermogravimetry analysis (TGA) was performed using a SDT-Q600 simultaneous TGA/DSC instrument at a heating rate of 5 °C min⁻¹ using α -Al₂O₃ as the reference. Raman spectra were obtained with a Bruker RFS 100/S spectrometer. N₂ adsorption–desorption isotherms were measured at liquid nitrogen temperature (77 K). Prior to measurement, the samples were degassed at 200 °C overnight. Surface areas were calculated by the multipoint Brunauer-Emmett-Teller (BET) method; total pore volumes were estimated from the volume adsorbed at a relative pressure (P/P_0) of 0.99, the pore-size distribution was calculated from the adsorption branch using the Barrett-Joyner-Halenda (BJH) method. X-ray photoelectron spectroscopy (XPS) spectra obtained with VG ESCA 2000 with a magnesium anode were used to demonstrate the content and the doping types of carbon, nitrogen, phosphorus and metal contents. All data were corrected using the C 1s peak at 284.8 eV as an internal standard.

Electrochemical Measurements

To have a good comparison of catalytic activity, the use amount of all catalysts are all the same. Taking CoP@NPMG electrode as an example, 4 mg of the catalyst was ultrasonically dispersed in the mixed solution of 0.9 mL of absolute ethyl alcohol and 0.1 mL of Nafion (5 wt%). The working electrode was prepared on a glassy carbon (GC) disk as the substrate. The GC electrode (5 mm in diameter) was first polished with 0.5 μ m down to 0.05 μ m alumina powder, washed with Mill-Q water and ethanol, and allowed to dry. 10 μ L of the obtained homogeneous catalyst ink was dropped onto the mirror polished glassy carbon electrode and allowed to dry in air, the

resulting electrode served as a working electrode. Ag/AgCl (saturated KCl) was used as the reference electrode, and the counter electrode was the graphite rod electrode. All the electrochemical experiments were conducted at room temperature on a CHI 660D electrochemical workstation. The current density was normalized to the geometrical surface area, and the resultant potentials were referenced to a reversible hydrogen electrode (RHE) by adding a value of $(0.205 + 0.059 \times \text{pH})$ V; all polarization curves were corrected for the iR compensation within the cell. The onset potential of the catalyst was obtained on the basis of the beginning of the linear part of the Tafel plots. EIS measurements were performed in potentiostatic mode from 0.1 to 100k Hz with an AC voltage of 10 mV. The accelerated stability tests were investigated by continuously cycling the potential between +0.05 V and -0.45 V versus RHE at a scan rate of 50 mV s^{-1} , while the time-dependent durability was operated at constant overpotential of 0.155 V.

HER activity evaluation: Linear sweep voltammetry with scan rate of 2 mV s^{-1} was taken in acid solution (0.5 M H_2SO_4), basic solution (1M KOH) and neutral solution (phosphate buffer solution: 1M $\text{K}_2\text{HPO}_4/\text{KH}_2\text{PO}_4$ PBS, pH=7) continuously purged with nitrogen with a rotating rate of 900 rpm during the test to remove hydrogen gas bubbles formed at the catalyst surface.

OER activity evaluation: Linear sweep voltammetry with scan rate of 2 mV s^{-1} was taken in both basic medium (1M KOH) and neutral medium (phosphate buffer solution: 1M PBS, pH=7), the oxygen was purged continuously at a rotating rate of 900 rpm during the test to remove oxygen gas bubbles formed at the catalyst surface.

Turnover Frequency Calculation: The number of active sites (n) was first examined employing cyclic voltammograms in 1 M PBS solution with a scan rate of 50 mV s^{-1} . Then the number of the voltammetric charges (Q) could be determined after deduction of the blank value. n

(mol) could be determined with the following equation:

$$n = \frac{Q}{2F(\text{HER})} \quad \text{equation (1)}$$

$$n = \frac{Q}{4F(\text{OER})} \quad \text{equation (2)}$$

Where F is Faraday constant (96500 C mol⁻¹). TOF could be calculated with the following equation:

$$TOF = \frac{I}{2 \times n \times F} = \frac{I}{Q(\text{HER})} \quad \text{equation (3)}$$

$$TOF = \frac{I}{4 \times n \times F} = \frac{I}{Q(\text{OER})} \quad \text{equation (4)}$$

where I (A) was the current of the polarization curve obtained by LSV measurements.

ECSA: Electrochemical capacitance measurements were used to determine the active surface area of catalyst. To measure the electrochemical capacitance, the potential was swept between 0.06 and 0.22 V vs RHE at different scan rates (10, 20, 40, 60, 80, 100 and 120 mV s⁻¹), where no faradaic process occurs. The capacitive currents were measured at 0.14 V vs RHE, plotted as a function of scan rate, and then a liner fit was used to determine the specific capacitance.

Mass Activity: The values of mass activity (A g⁻¹) were calculated using the following equation:

$$\text{mass activity} = \frac{j}{M}$$

Where j was the measured current density (mA cm⁻²) and M is the electrocatalyst loading amount (mg cm⁻²).

Faradaic Efficiency: The Faradaic efficiency of catalysts is defined as the ratio of the amount of the experimentally determined H₂ or O₂ to those of the theoretically expected H₂ or O₂ from the reaction, respectively. The experiments were conducted in a airtight cell. Before experiment, the electrolyte was bubbled with N₂ for at least 30 min. Then, the experiment was

carried out. As for the theoretical value, it was assumed that 100% current efficiency occurs during the reaction, which means only the HER or OER process was occurring at the electrode.

Proton adsorption measurements: The proton (H^+) adsorption measurements were performed according to the method in literature.⁵⁰ Then concentration of 5 mM HCl solution was selected and the adsorption experiments were conducted with a dialysis method. Typically, the CoP@NPMG catalyst solution was dialyzed using a semi-permeable membrane (MWCO 1000) in a 600 mL beaker, and the dialysate was 5 mM HCl (500 mL). If CoP@NPMG catalyst displays a good adsorption behaviour for H^+ , H^+ would gradually cross the semi-permeable membrane and dialyze into the CoP@NPMG catalyst solution. After stirring on a shaker for predetermined time intervals, the residual concentration of HCl solution was determined by titrating with 5 mM NaOH solution.

The amount of adsorbed H^+ (based on HCl), Q (g/g) is calculated by the following equation:

$$Q = \frac{(C_0 - C_e) \times V}{W}$$

Where C_0 and C_e are the initial and equilibrium concentration of HCl (mg/L), respectively; V is the volume of HCl solution (L) and W is the weight (mg) of CoP@NPMG adsorbent.

Water splitting test: The preparation of the working electrode was described below: the catalyst were dispersed in N-methyl-2-pyrrolidone solvent containing 7.5 wt% PVDF under sonication, in which the weight ration of the catalyst to PVDF is 8: 1. Then the slurry was coated onto a piece of 2 cm \times 1 cm carbon cloth, and occupied the area of 1 cm², the loading of catalyst was around 2.5 mg cm⁻².

DFT Computational Methods and Models.

Spin polarized density functional theory (DFT) calculations implemented with DMol3 module in

the Materials Studio program of Bio Accelrys were used for present study. The GGA method as implemented with Perdew, Burke, and Ernzerhof (PBE-GGA) was used to describe the exchange-correlation functional component of the Hamiltonian. Core treatment was adopted as DFT Semi-core Pseudopotentials to conduct metal relativistic effect. A double numerical plus polarization function basis sets were also used. A semi-empirical van der Waals correction accounted for the dispersion was included through the use of the DFT-D2 method of Grimme. A smearing of 0.006 Ha (1 Ha = 27.21 eV) to the orbital occupation was applied. The geometry convergence tolerance for energy change, max force and max displacement were 2×10^{-5} Ha, 0.004 Ha/Å, 0.005 Å, respectively. Self-consistent-field (SCF) procedures were performed with a convergence criterion of 1×10^{-6} Ha on the total energy to achieve accurate electronic convergence. $3 \times 3 \times 1$ Monkhorst-Pack grid k-points were employed for geometric optimization. In addition, the systems that involve Co were calculated with spin-polarization.

Figure S15 shows the model of CoP bulk, the lattice parameters are $a = 5.077$ Å, $b = 3.281$ Å and $c = 5.587$ Å. In present work, CoP (110) surface is modeled. We have constructed the correlative theoretical models to investigate the HER activity of CoP@NPMG composite (Figure S16). For comparative purpose, we also consider the composited CoP@Carbon (without dopants) and CoP systems. The top three layers of CoP (110) and graphene were allowed to relax, while the rest of CoP (110) (the bottom three layers) remained fixed.

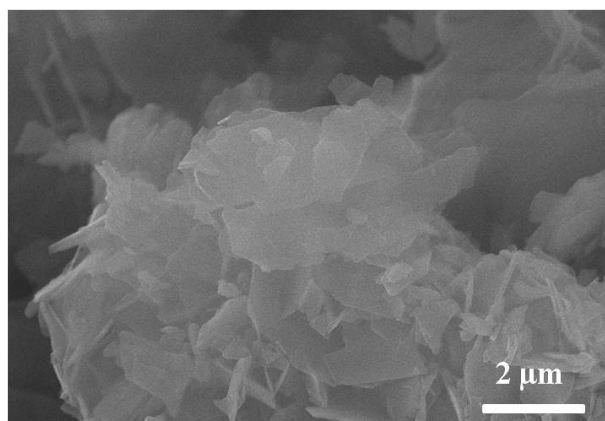


Fig. S1 SEM image of PA-melamine nanosheets.

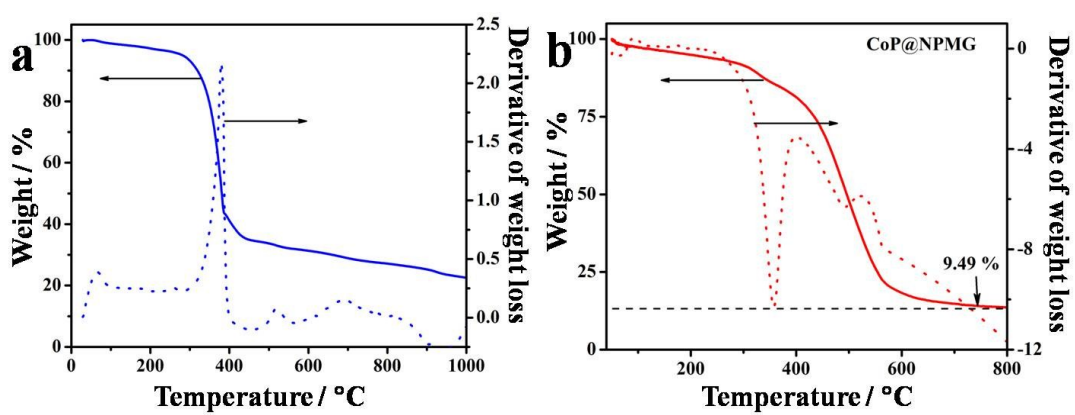


Fig. S2 TG profile of (a) the PA-melamine nanosheets coordinated with Co^{2+} cations in N_2 atmosphere and (b) CoP@NPMG in O_2 atmosphere.

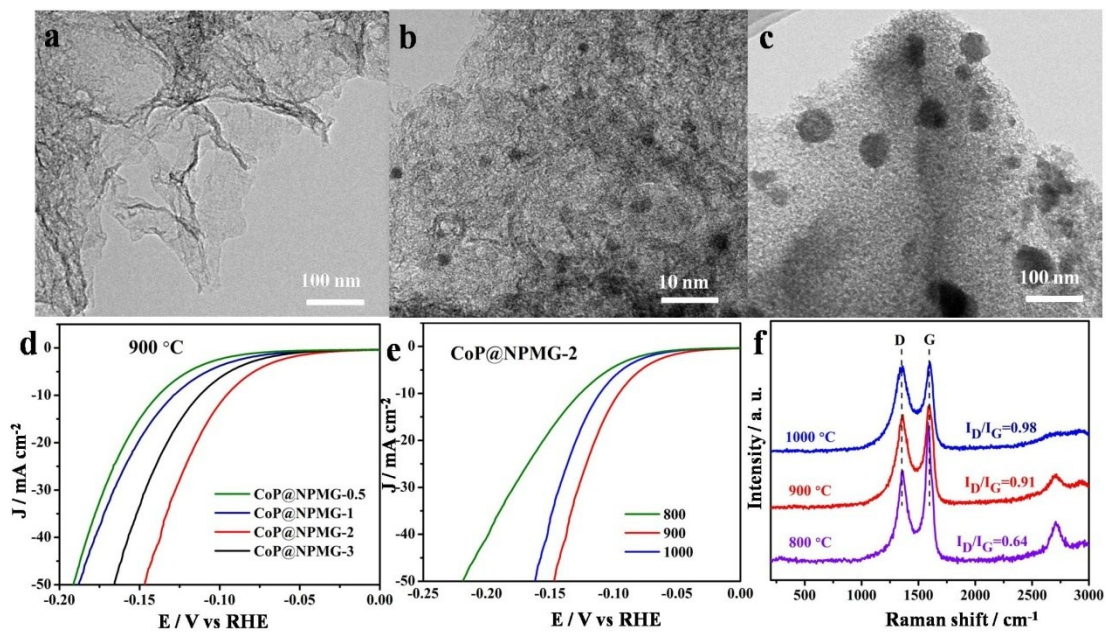


Fig. S3 (a) TEM image of CoP@NPMG-0.5. (b) TEM image of CoP@NPMG-1. (c) TEM image of CoP@NPMG-3. (d) Polarization curves for HER in 0.5 M H₂SO₄ for CoP@NPMG synthesized at 900 °C with different Co content. (e) Polarization curves for HER in 0.5 M H₂SO₄ for CoP@NPMG-2 prepared under various annealing temperature. (f) Raman spectrum of CoP@NPMG-2 prepared under various annealing temperature.

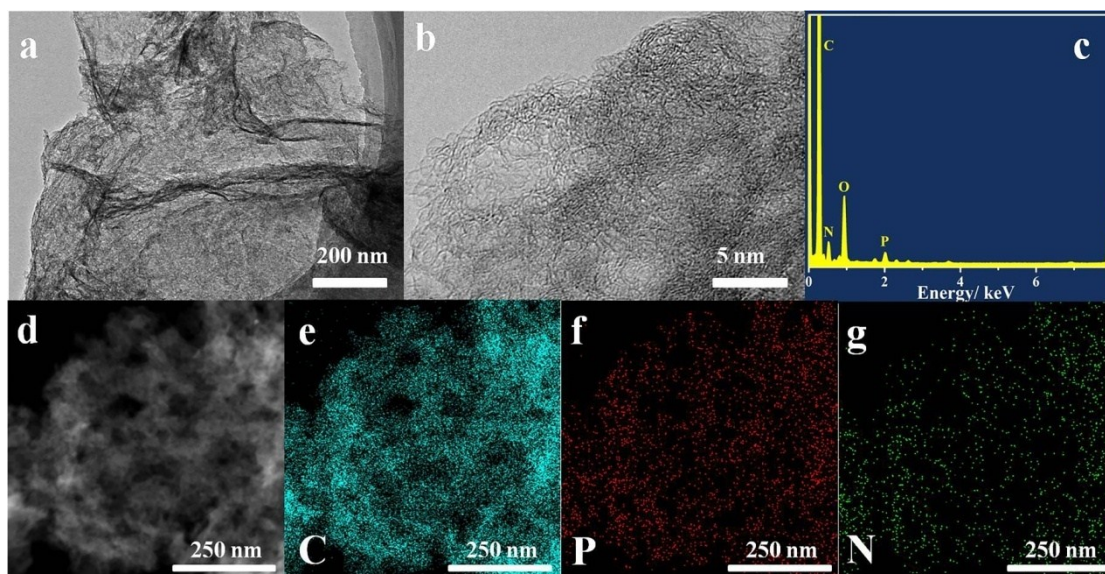


Fig. S4 (a)TEM and (b) HRTEM images of NPMG. (c) STEM-EDX spectrum of NPMG. (d-g) high-angle dark field STEM and corresponding EDX elemental mapping of C, P and N. The almost perfect images of C, P and N reveal that N and P atoms are distributed homogeneously over the graphene-like carbon sheet.

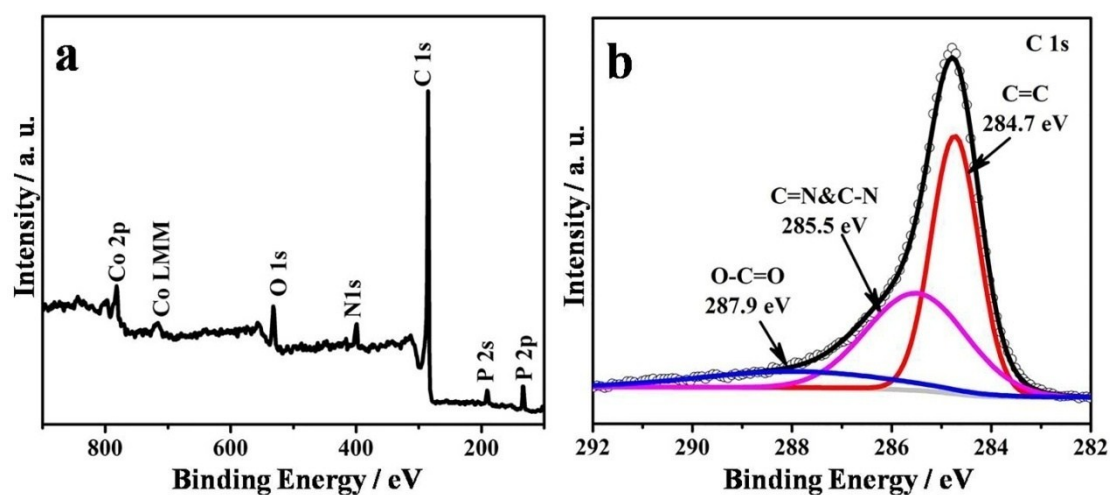


Fig. S5 (a) XPS spectrum of the pristine CoP@NPMG composite and (b) C 1s in CoP@NPMG. The high-resolution C 1s spectrum can be resolved into three contributions centered at 284.6 eV (sp^2 -hybridized graphitic C), 285.5 eV (N- sp^2 C), and 287.9 eV (O-C=O).

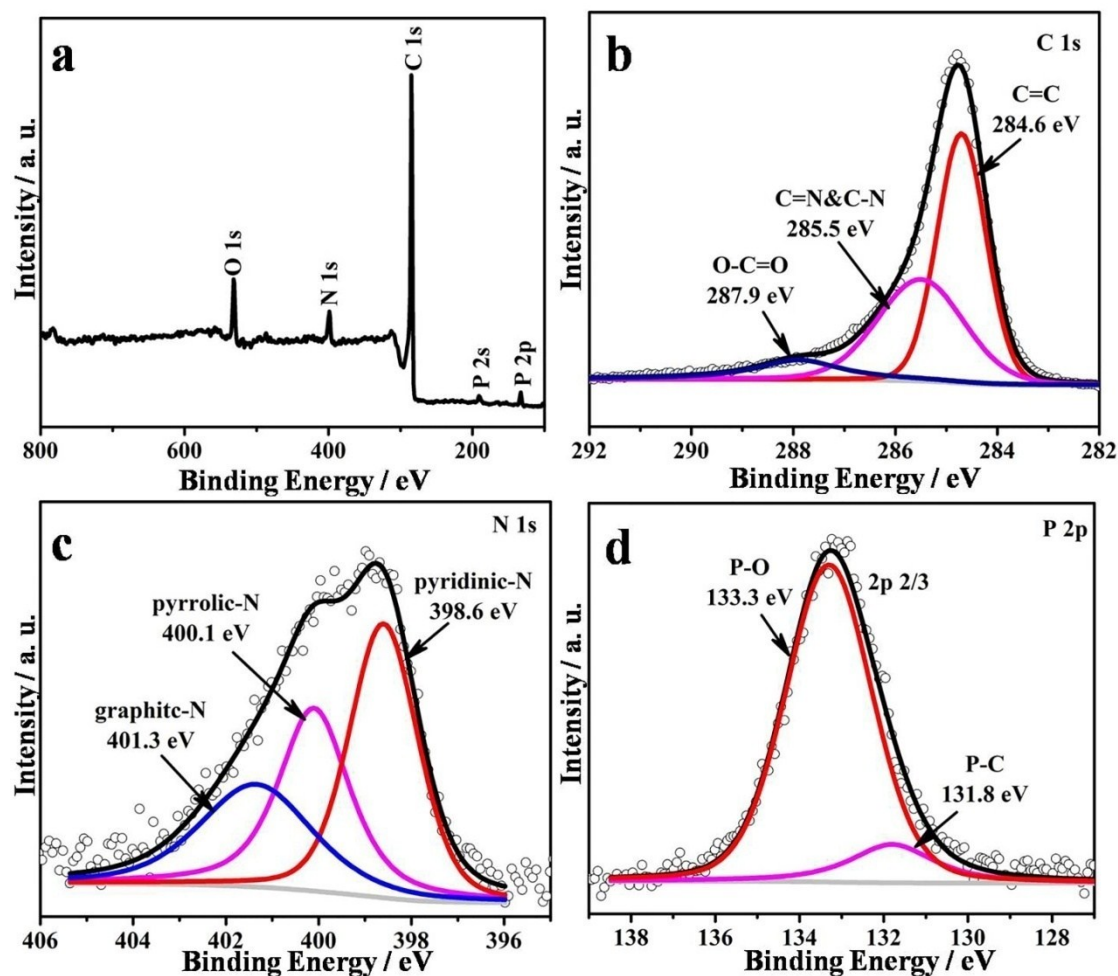


Fig. S6 (a) XPS spectrum of NPMG sample, and (b) C 1s, (c) N 1s and (d) P 2p core level in NPMG. The high-resolution C 1s spectra can be resolved into three contributions centered at 284.6 eV (sp^2 -hybridized graphitic C), 285.5 eV (N- sp^2 C), and 287.9 eV (O-C=O). Deconvolution of N 1s spectra reveals the presence of pyridinic-N (398.6 eV), pyrrolic-N (400.1 eV) and graphite-N (401.3 eV). For P 2p core level, a strong peak at 133.3 eV corresponds to phosphate-like structures that are bound to carbon lattices, and another peak at 131.8 eV is assigned to P-C.

Table S1. Element compositions of NPMG and CoP@NPMG samples.

	C at%	O at%	P at%	Co at%	N at%	Graphitic-N relative wt%	Pyridinic-N relative wt%	Pyrrolic-N relative wt%
NPMG	95.3 ^a	2.56	0.62	- ^c	1.52	42.1 ^d	31.6	26.3
	94.23 ^b	3.09	0.48	-	2.2			
CoP@NPMG	92.28 ^a	2.33	1.65	1.18	2.56	66.1 ^d	33.9	-
	89.22 ^b	4.12	2.13	1.43	3.1			

(a) Derived from SEM-EDS; (b) derived from XPS; (c) not detectable; (d) derived from XPS N 1s spectra.

Table S2. CoP loading value in CoP@NPMG.

	TGA	STEM-EDX
CoP loading	9.49 wt%	9.67 wt%

Table S3. BET surface area, BJH desorption pore size and BJH desorption pore volume for NPMG and CoP@NPMG samples.

	BET surface area	Mesopore size		Pore volume
	/ m ² g ⁻¹	/ nm		/ cm ³ g ⁻¹
NPMG	1084	4	7	0.32
CoP@NPMG	943	3.6	8	0.79

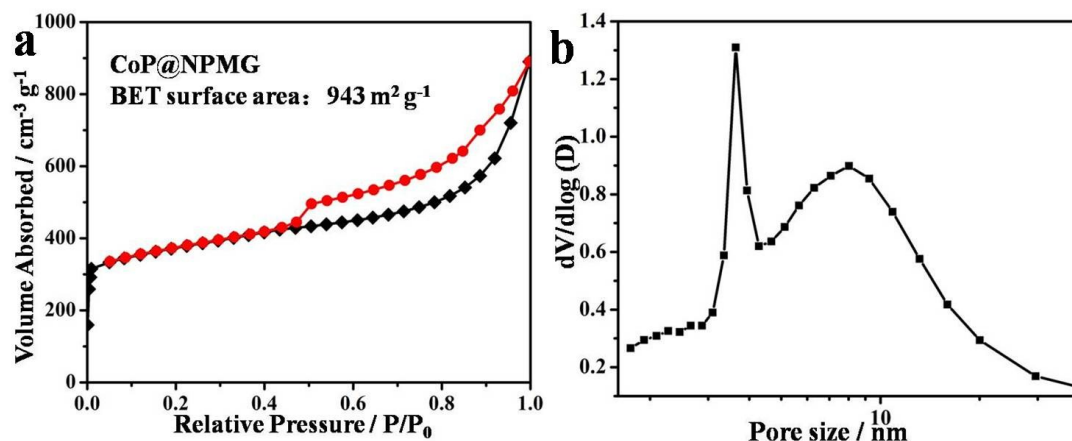


Fig. S7 (a) N₂ adsorption-desorption isotherm of the CoP@NPMG composite and (b) the corresponding pore size distribution curve. The rapid nitrogen uptake at lower N₂ pressures ($P/P_0 < 0.01$) confirms the coexistence of secondary porosity of mesoporous pores. The specific surface area for CoP@NPMG according to the Brunauer-Emmett-Teller (BET) calculation is determined to be 943 m²g⁻¹, the Barrett-Joyner-Halenda (BJH) distribution of the pore size centered at 3.6 nm and 8 nm confirms the mesoporous nature of CoP@NPMG.

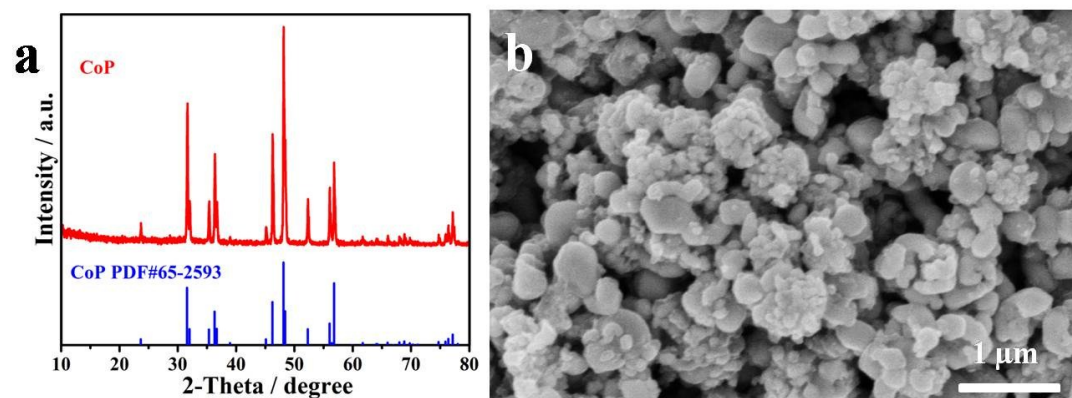


Fig. S8 (a) XRD pattern and (b) SEM image of CoP NPs.

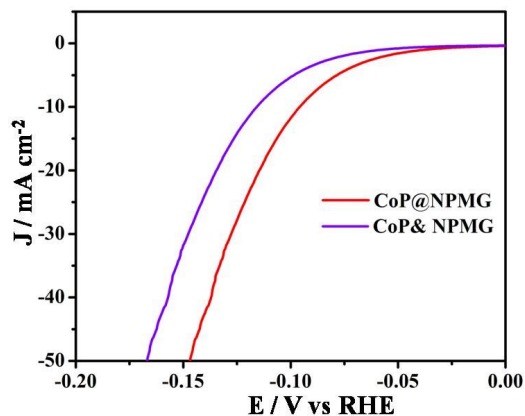


Fig. S9 Polarization curves for HER in 0.5 M H₂SO₄ of CoP@NPMG, and a mixture of CoP NPs and NPMG.

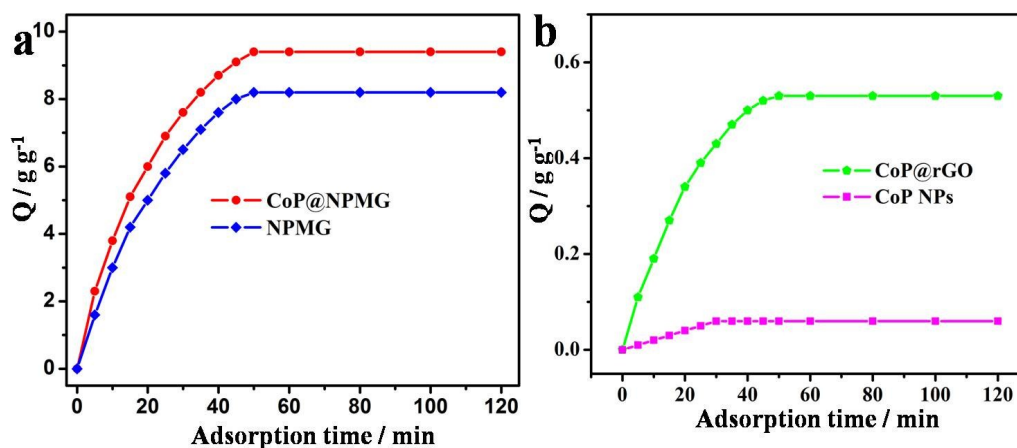


Fig. S10 (a) Dependence of adsorption time on the amounts of adsorbed H⁺ on CoP@NPMG and NPMG, and (b) dependence of adsorption time on the amounts of adsorbed H⁺ on CoP@rGO and CoP NPs.

According to the previous report,⁵⁰ the hydrogen ion activities around the catalyst has great influence on the activity of catalyst. As the H⁺ concentration around the catalyst increases, the HER reaction rate will increase. For CoP@NPMG catalyst, the strong adsorption proton capacity of N,P dual-doped graphitic carbon shell would enhance the proton concentration around CoP cores, thus resulting in the high HER performance of CoP@NPMG.

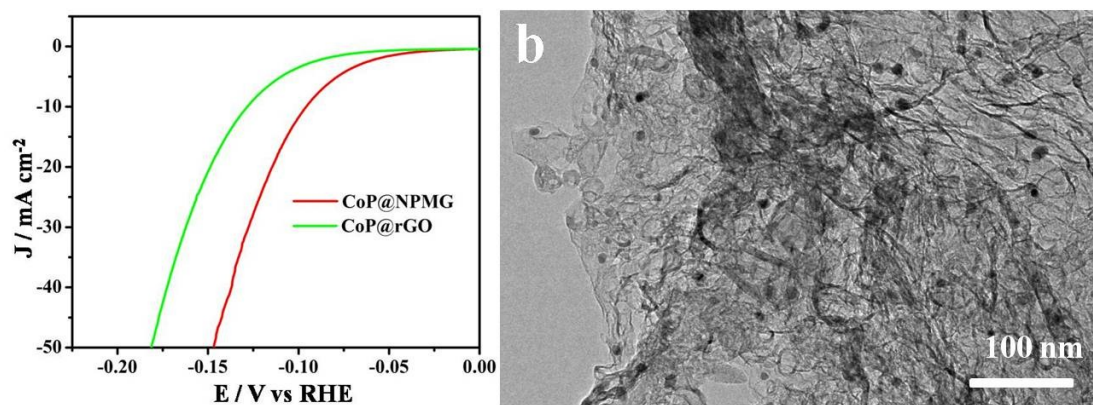


Fig. S11 (a) Polarization curves for HER in 0.5 M H_2SO_4 of CoP@NPMG and CoP@rGO, and (b) TEM image of CoP@rGO.

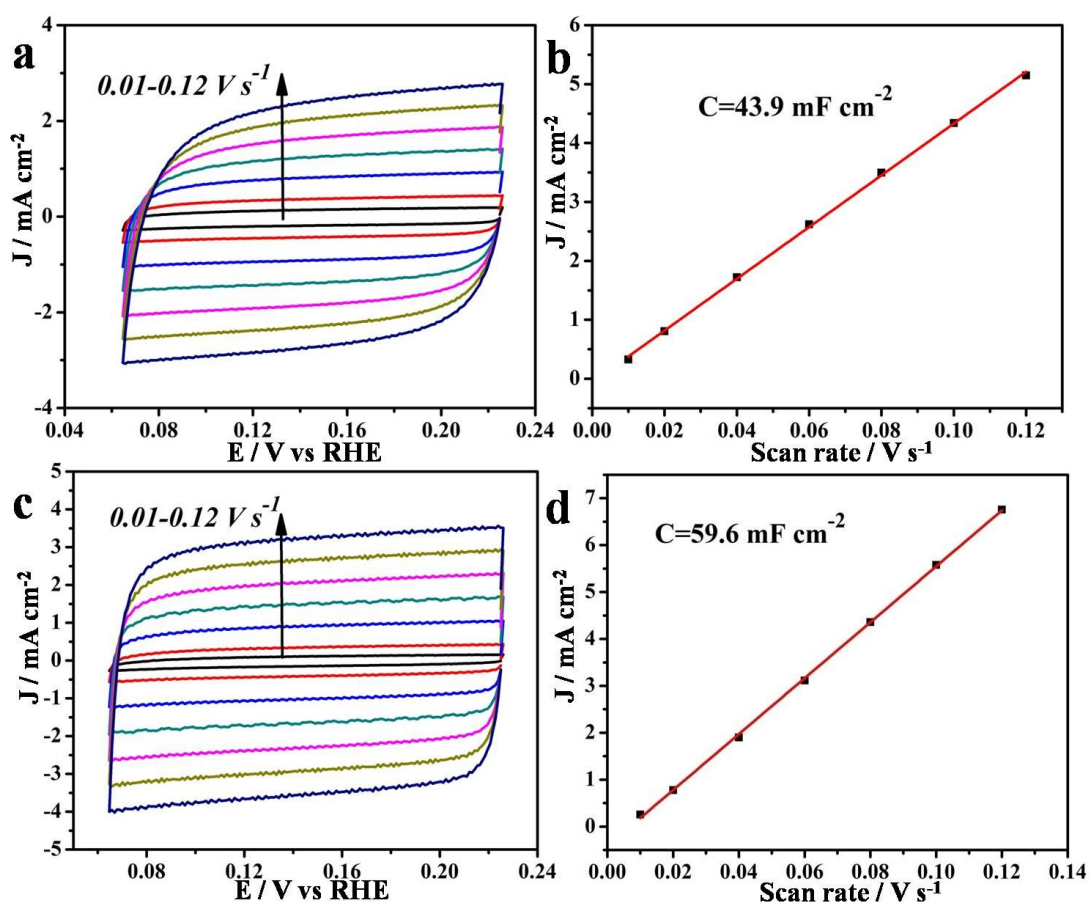


Fig. S12 (a) Cyclic voltammograms for NPMG at different scan rates from 0.01 to 0.12 V s^{-1} within the range of no faradaic reactions, and (b) variation of double-layer charging currents at 0.14 V as a function of scan rate. Symbols and the red solid line are experimental data from (a) and the fit liner, respectively. (c) Cyclic voltammograms for CoP@NPMG at different scan rates

from 0.01 to 0.12 V s⁻¹ within the range of no faradaic reactions, and (d) variation of double-layer charging currents at 0.14 V as a function of scan rate. Symbols and the red solid line are experimental data from (c) and the fit liner, respectively.

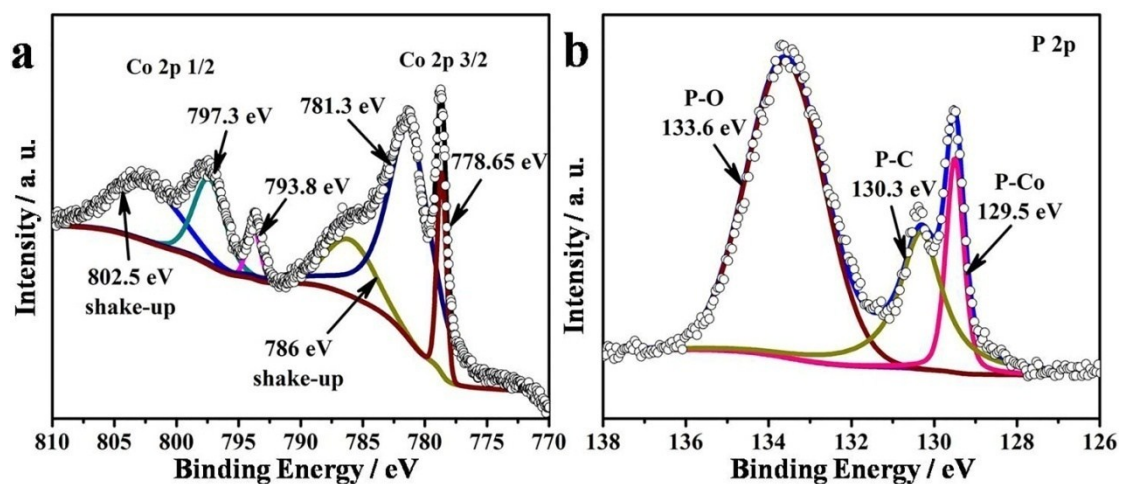


Fig. S13 XPS spectra of (a) Co 2p and (b) P 2p in CoP@NPMG composite after HER durability test in 1 M KOH.

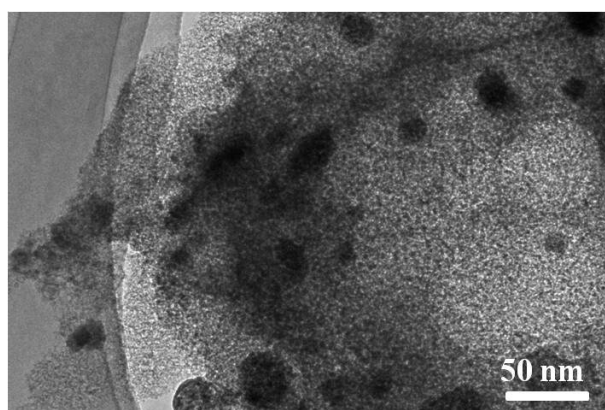


Fig. S14 TEM image of CoP@NPMG composite after HER process in 1 M KOH over 30 h.

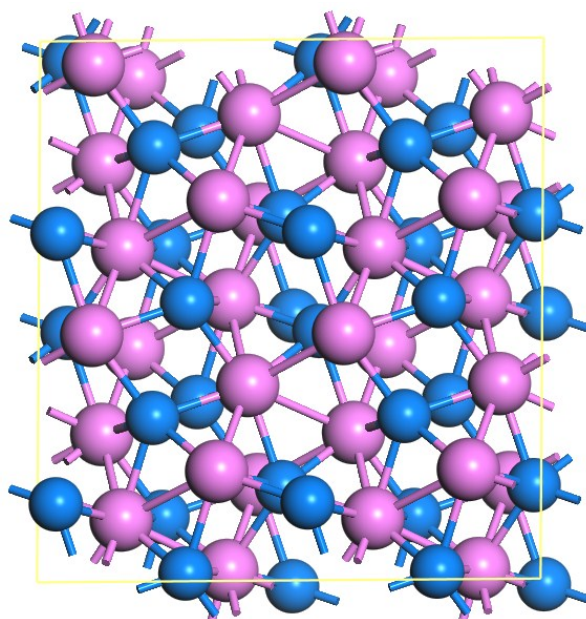
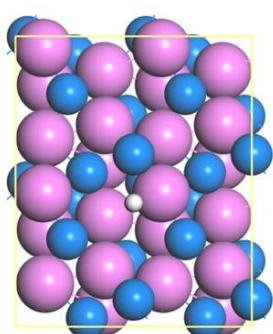
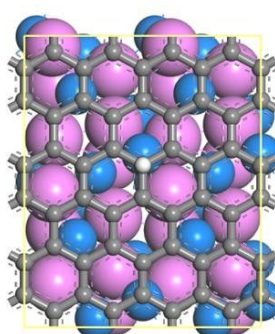


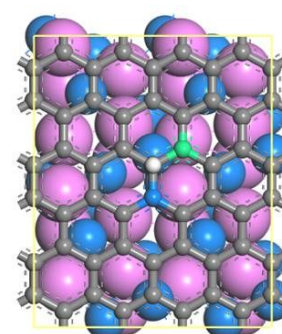
Fig. S15 The ball and stick model of CoP. The CoP crystallized in the orthorhombic system, space group $Pnma$, with the lattice constants $a= 5.077 \text{ \AA}$, $b= 3.281\text{\AA}$, $c= 5.587 \text{ \AA}$.



CoP
 $\Delta G_{H^*} = -0.66 \text{ eV}$



CoP@Carbon
 $\Delta G_{H^*} = 1.08 \text{ eV}$



CoP@NPMG
 $\Delta G_{H^*} = 0.10 \text{ eV}$

Fig. S16 The theoretical models of H adsorbed on: (a) CoP, (b) CoP@Carbon, (c) CoP@NPMG.

The grey, green, blue, violet and white balls represent C, N, P, Co and H atoms, respectively.

To compare the catalytic activity of different systems, the free energies of the intermediates were obtained by the equation $\Delta G(H^*) = \Delta E(H^*) + \Delta ZPE - T\Delta S$, where H^* denotes a H atom adsorbed on the surface and $\Delta E(H^*)$, ΔZPE and ΔS are the binding energy, zero point energy change and entropy change between the H adsorption and the gas phase, respectively. Therefore,

ΔZPE can be calculated as $\Delta ZPE = ZPE(H^*) - 1/2ZPE(H_2)$. ΔS can be got by the equation $\Delta S = S(H^*) - 1/2S(H_2) \approx -1/2 S(H_2)$, in view of the negligible vibrational entropy of H^* . Thus, we can easily conclude that the corresponding $T\Delta S$ is -0.205 eV, since $TS(H_2)$ is known to be 0.41 eV for H_2 at 300 K and 1 atm. Combining the analysis of Bader charge of atoms on the surfaces and the charge density difference (CDD) plotting, we selected several adsorption sites on each surface to investigate the capacity of H adsorption on different surfaces, involving one N atom (N site), one P atom (P site), several C sites adjacent to the N atom and one C site away from the N atom.

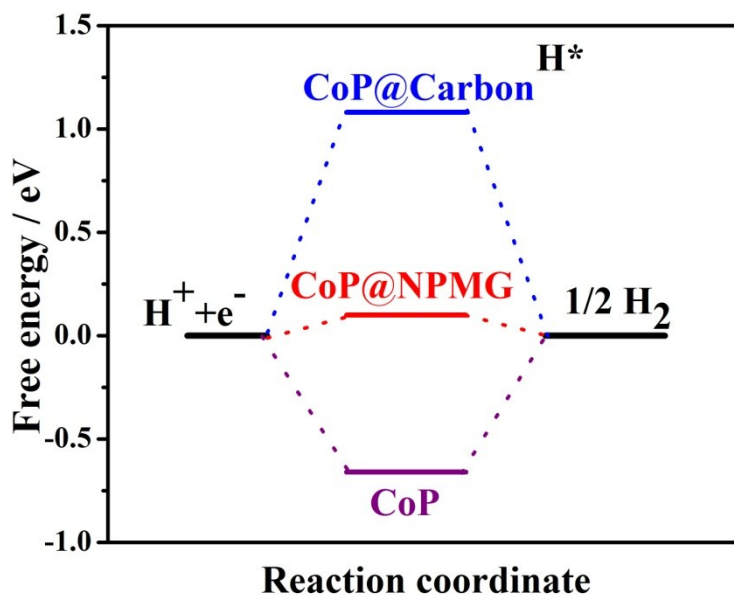


Fig. S17 The calculated free-energy diagram of the HER on various catalysts.

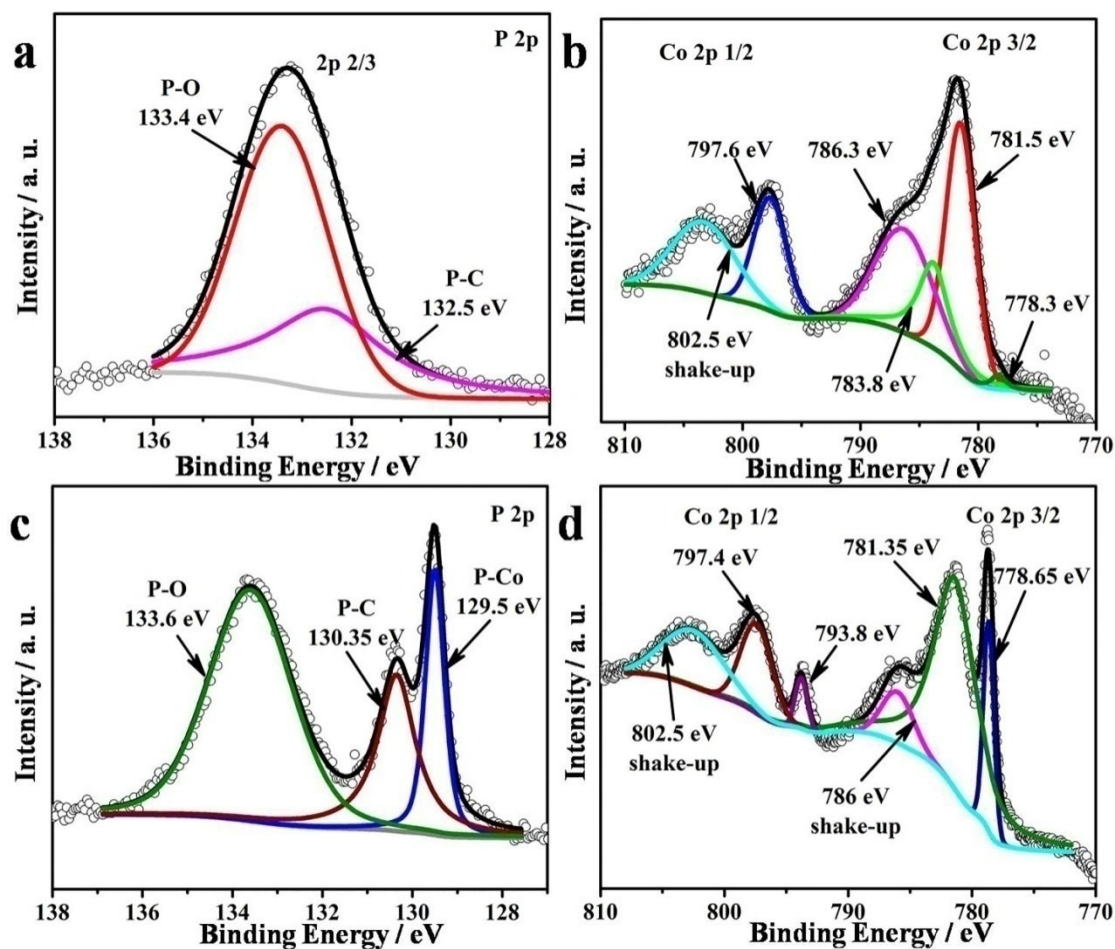


Fig. S18 XPS spectra ca. 5 nm of (a) P 2p and (b) Co 2p in CoP NPs sample after OER process in 1 M KOH, the intensities of peaks corresponding to CoP species in P 2p and Co 2p almost disappear, whereas the intensity of peak assigned to P-O in P 2p spectrum increase sharply. XPS spectra ca. 10 nm of (c) P 2p and (d) Co 2p in CoP composite after OER process in 1 M KOH, the spectrum of P 2p and Co 2p show similar peaks with pristine XPS measurement for CoP phase in CoP@NPMG, indirectly prove that the oxidation of partial CoP phase in CoP@NPMG sample takes place merely on the surface and the core remains CoP phase after OER process.

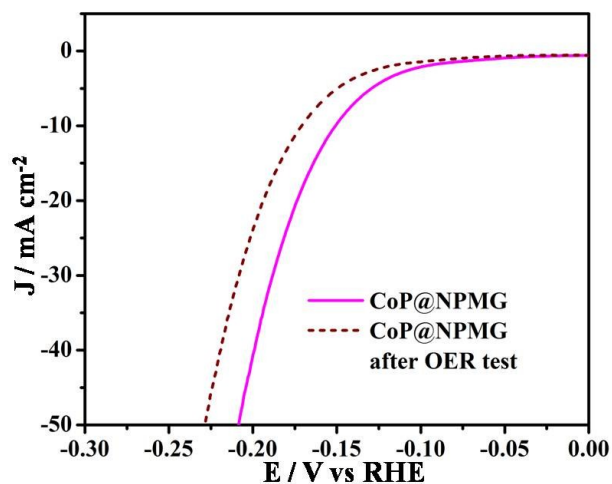


Fig. S19 HER activity of pristine CoP@NPMG and CoP@NPMG after OER test in 1 M KOH.

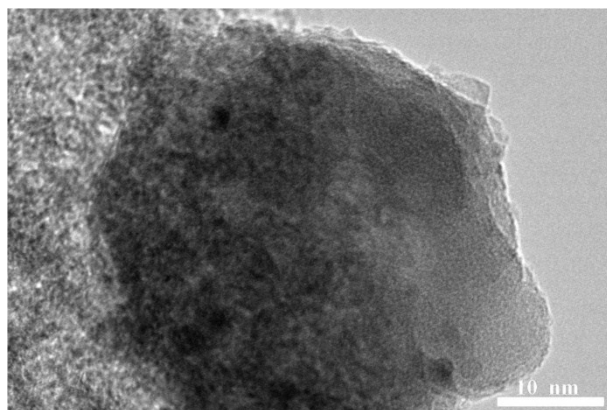


Fig. S20 TEM image of a single CoP nanoparticle in CoP@NPMG composite that are not completely encapsulated by carbon layers.

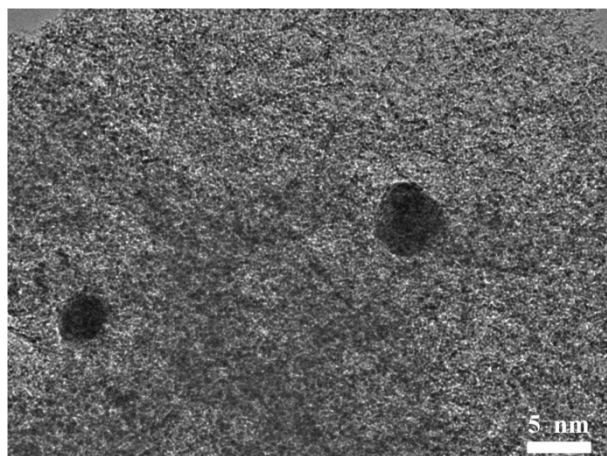


Fig. S21 TEM image of CoP@NPMG sample after OER durability test, suggesting that the morphology of sample remains after the long-term test.

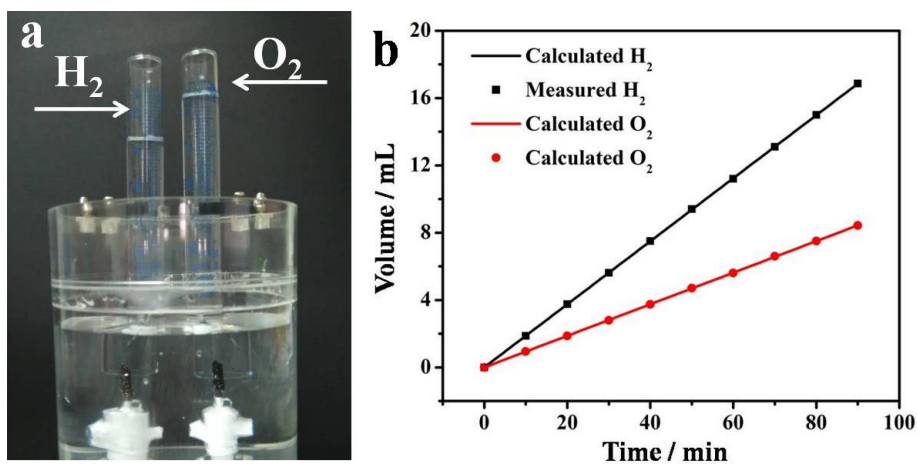


Fig. S22 (a) The optical image of experimental set-up of water displacement for collection of the evolved gas and (b) generated H_2 and O_2 volumes over time versus theoretical quantities assuming a roughly 100% Faradaic Efficiency for the overall water splitting of $CoP@NPMG||CoP@NPMG$ system in 1 M KOH at a constant current density of 25 mA cm^{-2} .

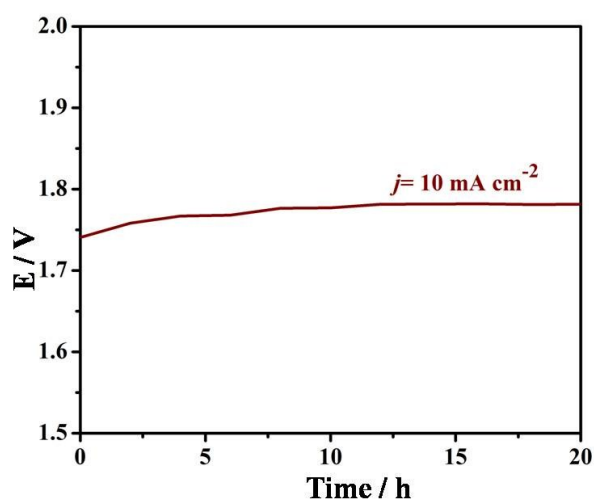


Fig. S23 Galvanostatic water electrolysis at a stationary current density of 10 mA m^{-2} over 20 h for $CoP@NPMG||CoP@NPMG$ in 1 M PBS.

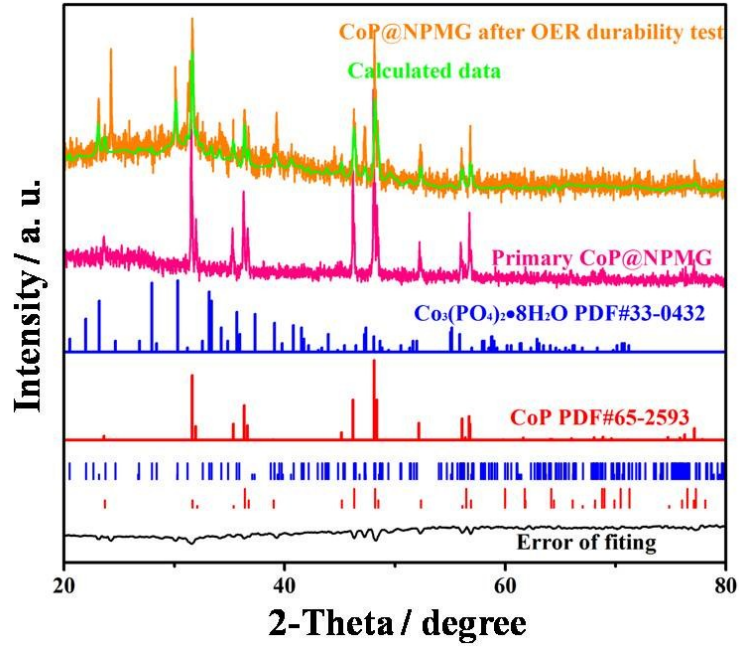


Fig. S24 Rietveld texture analysis from XRD diffraction spectra of primary CoP@NPMG and CoP@NPMG after OER durability test.

The XRD measurement was used to quantify the amount of cobalt oxides/hydroxides on the CoP nanoparticles in CoP@NPMG after the OER durability test. Due to the existence of P element, the Co element in cobalt oxides/hydroxides during OER process was present in the form of $\text{Co}_3(\text{PO}_4)_2 \cdot 8\text{H}_2\text{O}$ phase. Based on the refinement results, we obtained the weight percentage of CoP and $\text{Co}_3(\text{PO}_4)_2 \cdot 8\text{H}_2\text{O}$ was 65.63% and 34.37%, respectively. So the Moore mass ratio of Co element in CoP and $\text{Co}_3(\text{PO}_4)_2 \cdot 8\text{H}_2\text{O}$ was 10/3. Thus we can obtain that about 23 at% of whole Co element in CoP phase transform into cobalt oxides/hydroxides during OER process.

The technological detail of rietveld texture analysis can refer to Ref. S22.

Table S4. Selected summary of HER performance of some transition metal based core-shell composites or transition metal phosphides based catalysts, and compared with our work.

Materials	Electrolyte	$\eta@10\text{mA cm}^{-2}$ mV	Tafel slope (mV dec ⁻¹)	Reference
CoNx/C	0.5 M H ₂ SO ₄	133	57	S1
	1 M KOH	170	-	
	1 M PBS	247	-	
CoPS film on graphite	0.5 M H ₂ SO ₄	128	48	S2
FeP-GS	0.5 M H ₂ SO ₄	123	50	S3
FeP/NCNT	0.5 M H ₂ SO ₄	113	59	S4
Ni ₂ P/CNSs-40	0.5 M H ₂ SO ₄	92	46	S5
CoP/carbon	0.5 M H ₂ SO ₄	122	54	S6
CoP/rGO	0.5 M H ₂ SO ₄	260	104.8	S7
CoP/N-doped carbon	0.5 M H ₂ SO ₄	91	42	S8
Cobalt-phosphorous-derived films	1 M KOH	158	42	13
Co-P/N-doped carbon matrices	1 M KOH	154	51	S9
Fe-Co ₂ P/NCNTs	0.5 M H ₂ SO ₄	104	68	S10
Co-NRCNTs	1 M PBS	540	-	28
	1 M KOH	370	-	
CoP/CC	0.5 M H ₂ SO ₄	67	51	9
	1 M PBS	106	93	
	1 M KOH	209	129	
CoP@NPC	0.5 M H ₂ SO ₄	123	69	19
Co ₂ P@NPG	0.5 M H ₂ SO ₄	103	58	12
	1 M KOH	165	96	
NPMG	0.5 M H ₂ SO ₄	196	88	This work
CoP NPs	0.5 M H ₂ SO ₄	135	65	
CoP@NPMG	0.5 M H ₂ SO ₄	91	58	
	1 M PBS	126	62	
	1 M KOH	150	75	

Table S5. Selected summary of OER performance of some transition metal based core-shell composites or transition metal phosphides based catalysts, and compared with our work.

Materials	Electrolyte	$\eta@10\text{mA cm}^{-2}$ mV	Tafel slope (mV dec ⁻¹)	Reference
Cobalt-phosphorous-derived films	1 M KOH	345	47	13
Co-P/N-doped carbon matrices	1 M KOH	319	52	S9
CoP-CNT	1 M KOH	330	50	S11
CoP/TM	1 M KOH	310	87	S12
CoP hollow polyhedron	1 M KOH	300	57	S13
CoP NS/C	1 M KOH	277	85.6	S14
NiSe₂	1 M KOH	250	38	S15
IrO₂	1 M KOH	320	53	
CoP NPs/carbon	1 M KOH	320	71	15
CoP	1 M KOH	330	70	This work
CoP@NPMG	1 M KOH	276	54	
	1 M PBS	379	72	

Table S6. Comparison of the overall water splitting of some recently published results and our work.

Materials	Electrolyte	Voltage @10mA cm ⁻² mV	Reference
Co-P Co-P (Cobalt-phosphorous-derived films)	1 M KOH	1.65	13
Pt/C/TM RuO₂/TM	1 M KOH	1.57	S12
CoP/TM CoP/TM	1 M KOH	1.64	
CoP NPs/carbon CoP NPs/carbon	1 M KOH	1.587	15
CoP-MNA CoP-MNA	1 M KOH	1.62	39
Ni₂P/Ni/NF Ni₂P/Ni/NF	1 M KOH	1.49	47
NiSe NW/NF NiSe NW/NF	1 M KOH	1.63	S16
CoP_h/NG CoP_h/NG	1 M KOH	1.58	S17
NiCo₂S₄ NW/NF NiCo₂S₄ NW/NF	1 M KOH	1.63	S18
Ni₂P NPs/NF Ni₂P NPs/NF	1 M KOH	1.63	S12
EG/Co_{0.85}Se/NiFe-LDH EG/Co_{0.85}Se/NiFe-LDH	1 M KOH	1.67	S19
Ni_{2.3}%-CoS₂/CC Ni_{2.3}%-CoS₂/CC	1 M KOH	1.66	S20
Ni₅P₄ Ni₅P₄	1 M KOH	<1.7	S21
CoP@NPMG CoP@NPMG	1 M KOH	1.58	This work
CoP@NPMG CoP@NPMG	1 M PBS	1.74	

CoP NPs CoP NPs	1 M KOH	1.65	
------------------	---------	------	--

Reference:

- S1 H. W. Liang, S. Brüller, R. Dong, J. Zhang, X. Feng and K. Müllen, *Nat. Commun.*, 2015, **6**, 7992.
- S2 M. Cabán-Acevedo, M. L. Stone, J. R. Schmidt, J. G. Thomas, Q. Ding, H. C. Chang, M. L. Tsai, J. H. He and S. Jin, *Nature Mater.*, 2015, **14**, 1245-1251.
- S3 Z. Zhang, B. Lu, J. Hao, W. Yang and J. Tang, *Chemi. Commun.*, 2014, **50**, 11554-11557.
- S4 Q. Liu, Z. Pu, A. M. Asiri and X. P. Sun, *Electrochim. Acta*, 2014, **149**, 324-329.
- S5 Y. Pan, Y. Liu and C. Liu, *J. Power Sources*, 2015, **285**, 169-177.
- S6 Q. Liu, J. Tian, W. Cui, P. Jiang, N. Cheng, A. M. Asiri and X. P. Sun, *Angew. Chem.*, 2014, **126**, 6828-6832.
- S7 L. Ma, X. Shen, H. Zhou, G. Zhu, Z. Ji and K. Chen, *J. Mater. Chem. A*, 2015, **3**, 5337-5343.
- S8 Z. Zhang, J. Hao, W. Yang and J. Tang, *ChemCatChem*, 2015, **7**, 1920-1925.
- S9 B. You, N. Jiang, M. Sheng, S. Gul, J. Yano and Y. Sun, *Chem. Mater.*, 2015, **27**, 7636-7642.
- S10 Y. Pan, Y. Liu, Y. Lin and C. G. Liu, *ACS Appl. Mat. Interfaces*, 2016, **8**, 13890-13901.
- S11 C. C. Hou, S. Cao, W. F. Fu and Y. Chen, *ACS Appl. Mat. Interfaces*, 2015, **7**, 28412-28419.
- S12 L. Yang, H. Qi, C. Zhang and X. P. Sun, *Nanotech.*, 2016, **27**, 23LT01.
- S13 M. Liu and J. Li, *ACS Appl. Mat. Interfaces*, 2016, **8**, 2158-2165.
- S14 J. Chang, L. Liang, C. Li, M. Wang, J. Ge, C. Liu and W. Xing, *Green Chem.*, 2016, **18**, 2287-2295.
- S15 I. H. Kwak, H. S. Im, D. M. Jang, Y. W. Kim, K. Park, Y. R. Lim, E. H. Cha and J. Park, *ACS Appl. Mat. Interfaces*, 2016, **8**, 5327-5334.
- S16 C. Tang, N. Cheng, Z. Pu, W. Xing and X. Sun, *Angew. Chem, Int. Ed.*, 2015, **54**, 9351-9355.
- S17 X. Yu, S. Zhang, C. Li, C. Zhu, Y. Chen, P. Gao, L. Qi and X. Zhang, *Nanoscale*, 2016, **8**, 10902-10907.
- S18 A. Sivanantham, P. Ganesan and S. Shanmugam, *Adv. Func. Mater.*, 2016, **26**, 4661-4672.
- S19 Y. Hou, M. R. Lohe, J. Zhang, S. Liu, X. Zhuang and X. Feng, *Energy Environ. Sci.*, 2016, **9**, 478-483.
- S20 W. Fang, D. Liu, Q. Lu, X.P. Sun and A. M. Asiri, *Electrochem. Commun.*, 2016, **63**, 60-64.
- S21 M. Ledendecker, S. Krick Calderón, C. Papp, H. P. Steinrück, M. Antonietti and M. Shalom, *Angew. Chem.*, 2015, **127**, 12538-12542.
- S22 L. Lutterotti, M. Bortolotti, G. Ischia, I. Lonardelli and H.-R. Wenk, *Z. Kristallogr. Suppl.*, 2007, **26**, 125-130.